



Direct Z-scheme ZnO/CdS hierarchical photocatalyst for enhanced photocatalytic H₂-production activity

Sheng Wang^a, Bicheng Zhu^a, Mingjin Liu^a, Liuyang Zhang^{a,*}, Jiaguo Yu^{a,*}, Minghua Zhou^{b,*}

^a State Key Laboratory of Advanced Technology for Materials Synthesis and Processing, Wuhan University of Technology, Wuhan, 430070, China

^b Hubei Key Laboratory of Wudang Local Chinese Medicine Research, Hubei University of Medicine, Shiyan, 442000, China

ARTICLE INFO

Keywords:

ZnO
CdS
Hierarchical structure
Photocatalytic H₂-production
Direct Z-scheme

ABSTRACT

Herein, ZnO/CdS hierarchical composite was prepared through a hydrothermal and chemical bath deposition (CBD) process. Its photocatalytic H₂-production performance was tested. Mass ratio of CdS acted a pivotal part in light absorption and photocatalytic properties. Noticeably, promoted photocatalytic H₂-production activity of 4134 $\mu\text{mol g}^{-1} \text{h}^{-1}$ was achieved by the sample with optimal CdS content. Significantly, the photoluminescence (PL) detection of hydroxyl radicals, as well as the *in-situ* XPS measurements was selected to verify the direct Z-scheme charge migration mechanism. This mechanism endowed the composite with strong capability for hydrogen evolution and elucidated the improved photocatalytic performance. The improvement of photocatalytic activity was due to hierarchical structure, extended visible light response and direct Z-scheme mechanism. This work will give an innovative vision in constructing direct Z-scheme photocatalytic system with great photocatalytic H₂-production activity.

1. Introduction

With the development of society, human's life is plagued by increasingly grave energy issues [1–5]. Exploration of clean energy source such as hydrogen becomes imminent. Encouraged by the successful hydrogen generation over TiO₂ discovered by Fujishima for the first time, photocatalytic hydrogen production opens new possibilities [6]. This method can store the sustainable solar energy into hydrogen without secondary pollution. Against this background, the development of H₂-production photocatalysts has attracted attention throughout the world [7–12].

Among semiconductors, zinc oxide (ZnO), due to its stability, non-toxicity and affordability, has been thoroughly studied in solar cells [13], adsorption [14] and photocatalysis [15–17]. However, pristine ZnO itself does not show high photocatalytic H₂-production rate, mainly restricted by its low conduction band position and wide bandgap. Comparatively, cadmium sulfide (CdS) is visible-light-active [18–22]. Pitifully, it suffers from photocorrosion [23–25]. In view of their pros and cons, we aimed to find a way out of the difficulty in adopting a single material as the photocatalytic H₂-production catalyst. Heterojunction formation of ZnO and CdS can ensure complementarity and mutual reinforcement. This approach has been testified many times [26–31]. For example, core-shell CdS@TiO₂ showed enhanced photocatalytic performance for H₂ production [32].

Considering the analysis beforehand [3,33–35], ZnO is an oxidation photocatalyst which possesses low valance band (VB) position and exhibits strong oxidation ability, whereas CdS is a reduction photocatalyst with high conduction band (CB) position displaying strong reduction ability. The suitable matching of their band structure has a very good chance of constructing direct Z-scheme photocatalyst [15,36]. Unlike the traditional Type-II mechanism, in direct Z-scheme mechanism, electrons (e⁻) in the higher CB (conduction band) and the holes (h⁺) in the lower VB (valence band) are maintained, which preserves stronger reduction abilities of electrons and oxidation abilities of holes [37–41]. Apart from this advantage, direct Z-scheme photocatalyst can accelerate the charge migration and promote charge separation. The superiority of direct Z-scheme system has been showcased lately. For instance, Peng and co-workers fabricated a direct Z-scheme g-C₃N₄/WO₃ photocatalyst, demonstrated that photoinduced electrons migrated from WO₃ CB to C₃N₄ VB [42]. Grela *et al.* constructed a Cu₂O/TiO₂ Z-scheme photocatalyst, which protected Cu₂O from photocorrosion [43]. These direct Z-scheme systems exhibited strong reduction ability of electrons and oxidation ability of holes, leading to superior photocatalytic performance.

Herein, ZnO/CdS hierarchical composite photocatalyst was assembled through facile chemical bath deposition (CBD). The effect of CdS ratio on the photocatalytic performance was well scrutinized. The ZnO/CdS with optimized CdS ratio at 30.9% had enhanced

* Corresponding authors.

E-mail addresses: zly2017@whut.edu.cn (L. Zhang), jiaguoyu@yahoo.com (J. Yu), zmhsy2000@hbm.edu.cn (M. Zhou).

<https://doi.org/10.1016/j.apcatb.2018.10.019>

Received 10 June 2018; Received in revised form 1 October 2018; Accepted 7 October 2018

Available online 09 October 2018

0926-3373/ © 2018 Elsevier B.V. All rights reserved.

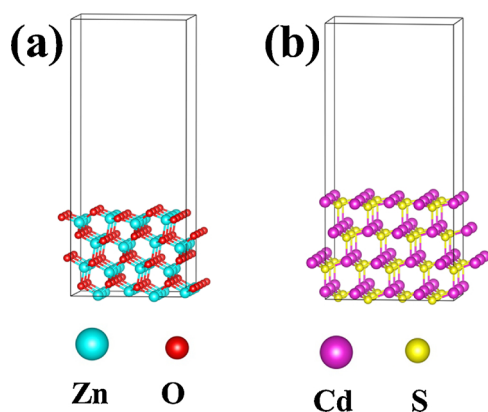


Fig. 1. Geometric structures of (a) ZnO (101) and (b) CdS (111) surfaces. The cyan, red, pink, and yellow spheres stand for Zn, O, Cd and S atoms, respectively (For interpretation of the references to colour in this figure legend, the reader is referred to the web version of this article).

photocatalytic H_2 -production performance. Of note, the performance improvement was expounded by direct Z-scheme mechanism, which was justified by the *in-situ* XPS characterization and the theoretical simulation by density functional theory (DFT).

2. Experimental

2.1. Materials

Zinc acetate dihydrate ($\text{Zn}(\text{Ac})_2 \cdot 2\text{H}_2\text{O}$), trisodium citrate dihydrate ($\text{Na}_3\text{C}_6\text{H}_5\text{O}_7 \cdot 2\text{H}_2\text{O}$), urea ($\text{CO}(\text{NH}_2)_2$), thioacetamide (CH_3CSNH_2) and cadmium chloride (CdCl_2) were purchased and used without purification (Fig. 1).

2.2. Preparation of ZnO/CdS hierarchical microsphere

Typically, 3.75 mmol $\text{Zn}(\text{Ac})_2 \cdot 2\text{H}_2\text{O}$, 15 mmol $\text{CO}(\text{NH}_2)_2$ and 0.75 mmol $\text{Na}_3\text{C}_6\text{H}_5\text{O}_7 \cdot 2\text{H}_2\text{O}$ were dissolved and sonicated in 80 mL of water to form a homogeneous solution. The obtained clear solution was then placed in a 100 mL Teflon-lined stainless steel autoclave, which was sealed and maintained at 120 °C for 6 h. The resulting precipitates were collected by centrifugation and drying. Finally, after calcination at 300 °C for 2 h, ZnO powders were gained, and labeled as Z. The ZnO/CdS composites were synthesized by chemical bath deposition. Firstly, 0.2 mmol CdCl_2 and 0.2 mmol CH_3CSNH_2 were dissolved separately in 20 mL of water. Then, the solution was mixed and 0.1 g as-prepared ZnO powders were added. Afterwards, the container was kept at 40 °C for 20 min for the reaction proceeding. Finally, the ZnO/CdS sample was collected by centrifugation and dried in vacuum. The as-prepared ZnO/CdS was labeled as ZC-3, and the synthesis of other ZnO/CdS samples was similar to that of ZC-3 except that the concentrations of the sources were varied. The respective amount of the precursors in the hybrid preparation and the corresponding abbreviation are shown in Table 1. Besides, commercial CdS was labeled as C.

Table 1

The amounts of precursors in preparing ZnO/CdS hybrids.

Sample	ZnO (mg)	CdCl_2 (mmol)	CH_3CSNH_2 (mmol)
ZC-1	100	0.05	0.05
ZC-2	100	0.1	0.1
ZC-3	100	0.2	0.2
ZC-4	100	0.4	0.4

2.3. Characterization

X-ray diffraction (XRD) results were obtained with an X-ray diffractometer (D/Max-RB, Rigaku, Japan). Microstructure was observed on a scanning electron microscope (SEM) (JSM-7500) and a transmission electron microscope (TEM) (JEM-2100 F). The pore structure and surface area were investigated on a nitrogen (N_2) adsorption apparatus (ASAP 3020, USA). The mass ratio of CdS in the composite sample was measured on a plasma–optical emission apparatus (Prodigy). The optical properties were recorded on a UV–vis spectrometer (UV-2600). X-ray photoelectron spectroscopy (XPS) spectra were recorded with a Thermo ESCALAB 250Xi apparatus. As for the *in-situ* XPS characterization, a low-power 365 nm LED light (Shenzhen LAMPLIC Science Co. Ltd., China) was placed ca. 20 cm away from the prepared samples during the normal XPS characterization to investigate the electron density changes on prepared samples under light irradiation. The hydroxyl radical ($\cdot\text{OH}$) was measured by a fluorescence spectrophotometer (F-7000) (Hitachi, Japan). To be specific, 0.05 g samples were dispersed into 20 mL of mixed solutions (5×10^{-4} M terephthalic acid in 2×10^{-3} M NaOH solution). After 1 h light illumination, the solution was centrifuged. Then the PL intensities were recorded and the quantity of hydroxyl radicals can be reflected by the PL intensity.

2.4. Photocatalytic and photoelectrochemical measurements

The photocatalytic H_2 -production performance was evaluated in a flask and a 350 W Xenon lamp was selected as light source. To be specific, 50 mg of the sample was dispersed into 80 mL of mixed solution (0.35 M Na_2S and 0.25 M Na_2SO_3). Before light illumination, the flask was pumped by N_2 for 0.5 h to remove air. After 1 h illumination, 400 μL gaseous products were extracted from the flask then measured by gas chromatography (GC-14C, Japan). Transient photocurrent response results were recorded with an electrochemical workstation (CHI660C) including a Ag/AgCl reference electrode, a Pt wire counter electrode and a working electrode. The working electrode was prepared by coating the sample on a piece of FTO glass with an active area of ca. 1 cm^2 , and the light source was a 3 W LED (365 nm). A 0.4 M Na_2SO_4 solution was selected as the electrolyte. The electrochemical impedance spectroscopy (EIS) results were measured on the same system above. The system was applied a bias (open circuit voltage) and measured over a frequency range (0.05–10⁵ Hz) with an AC amplitude (10 mV).

2.5. Computational details

Density functional theory (DFT) was calculated using the CASTEP module. The Perdew – Burke – Ernzerhof (PBE) exchange-correlation functional was selected within the generalized gradient approximation (GGA). A cutoff energy of 340 eV was used. The convergence tolerance for the energy and force was set at 1.0×10^{-5} eV/atom and 0.03 eV/Å, respectively. After geometry optimization, the average potential profile was calculated to obtain the work functions of CdS (111) and ZnO (101) models (their geometric structures are shown in 1). The work function (Φ) is defined as $\Phi = E_{\text{vac}} - E_{\text{F}}$ (E_{vac} : vacuum energy, E_{F} : Fermi energy).

3. Results and discussion

3.1. Phase structures and morphology

Fig. 2 shows the X-ray diffraction patterns of bare ZnO and ZnO/CdS composites with different ratios. For pristine ZnO (Z), 7 distinct diffraction peaks appear at around 31.8°, 34.4°, 36.3°, 47.5°, 56.6°, 62.9° and 67.9°, which can be matched with those of ZnO (JCPDS No. 36-1451) [44,45]. For ZnO/CdS composites with different CdS portions, apart from the characteristic peaks of ZnO, an additional hump can be observed at around 26.5°, corresponding to the (111) crystal facet of cubic CdS (JCPDS No. 80-0019), indicating that the CdS nanoparticles

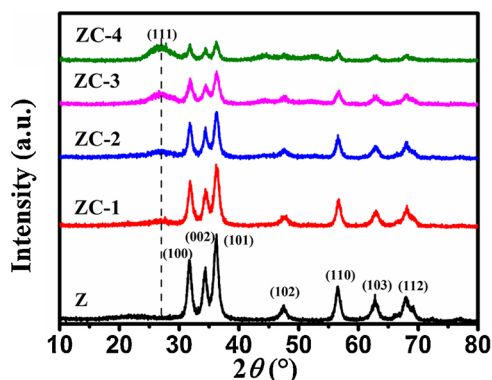


Fig. 2. XRD patterns of as-prepared ZnO and ZnO/CdS composite samples.

have been successfully deposited on the ZnO surface [46]. It can be easily seen in Fig. 2, as the Cd source and S source increase (from ZC-1 to ZC-4), the peak intensities belonging to CdS gradually strengthen whereas those of ZnO gradually weaken, reflecting the increased mass ratio of CdS in the composite.

From the FESEM image (Fig. 3), we can see that the morphology of the as-prepared ZnO sample displays a hierarchical microsphere structure composed of nanosheets, and the size distribution is relatively uniform within the range of 4–5 μm . Whereas, from the FESEM image of a typical composite, it can be found that it well inherits the microsphere structure of bare ZnO and newly-formed nanoparticles (NPs) are distributed on the surface. The small and homogeneous NPs are attached to the surface of ZnO. The NPs are determined to be CdS through integrating the XRD results. By examining Fig. 3b and d, the rough surface proves the presence of CdS.

The microstructure of sample ZC-3 was further investigated by TEM and HRTEM. As shown in Fig. 4a, the TEM images are consistent with the FESEM ones. The microspheres consist of nanosheets. Particularly, some NPs are anchored on the surface. In the HRTEM image (Fig. 4b), the crystal lattice fringes are relatively clear, suggesting its good crystallinity. The calculated lattice spacing of 0.247 nm is indexed to the

(101) plane of ZnO while another lattice spacing of 0.335 nm is indexed to the (111) plane of CdS. [47,48]. Fig. 4e–f shows the EDS mapping images of sample ZC-3, which prove the existence of Zn, O, Cd, and S elements. Combining TEM and EDS results, the denser distribution of Cd and S on the periphery of the spheres verifies the successful deposition of CdS on the ZnO surface.

3.2. Textural properties

Fig. 5 shows the N_2 adsorption-desorption isotherms for different samples, with the inset showing the pore size distribution of them. The isotherms are close to the Y-axis at the lower pressure region, which indicates that they have stronger interaction with nitrogen. Besides, hysteresis loops at higher pressure region are exhibited for all of the five samples. Therefore, the isotherms are categorized as type IV with H3 hysteresis loops [33,34], which denote that slit-type pores are formed by a large number of flaky lamella [49,50]. From the pore size distribution of all the samples (Fig. 5 inset), wide distribution is witnessed (2–250 nm). Apparently, after the loading of CdS, both the specific surface area and the average pore size increase (Table 2), whereas the ratio of large mesopores decreases (Fig. 5 inset). This is due to that some small mesopores are blocked by CdS NPs. In general, the enlargement of the specific surface area can provide more active sites for catalytic reactions (Table 2) [51,52].

3.3. Light absorption

The DRS spectra of sample Z and ZC are shown in Fig. 6. We can see that all samples show a light absorption threshold at about 385 nm, corresponding to the intrinsic absorption of ZnO [53]. As for the composite sample, a significant increase in the visible light region (400–500 nm) emerges, which is mainly due to the successful loading of CdS [54,55]. Besides, we estimate the bandgap of cubic CdS to be 2.3 eV based on the intersection with abscissa axis of the adsorption edge of ca. 550 nm [36]. In addition, the absorption edge has a distinct red-shift, which is due to the gradual increase of CdS loading. With the aid of CdS, the hybrid sample demonstrates an enhanced visible-light

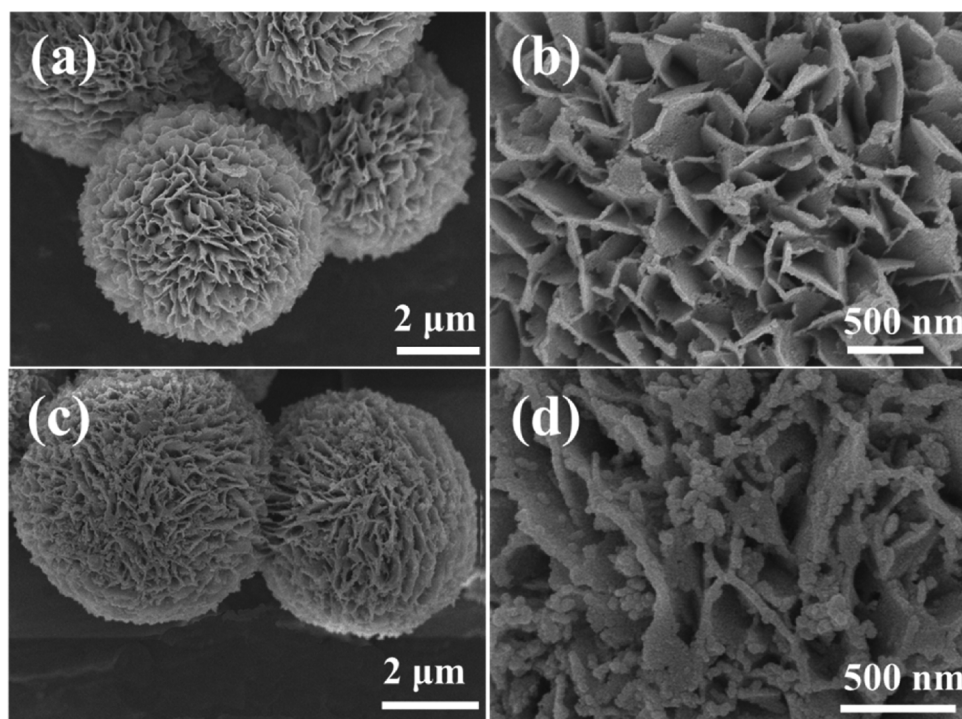


Fig. 3. FESEM images with different magnifications of (a,b) ZnO and (c,d) ZnO/CdS (ZC-3).

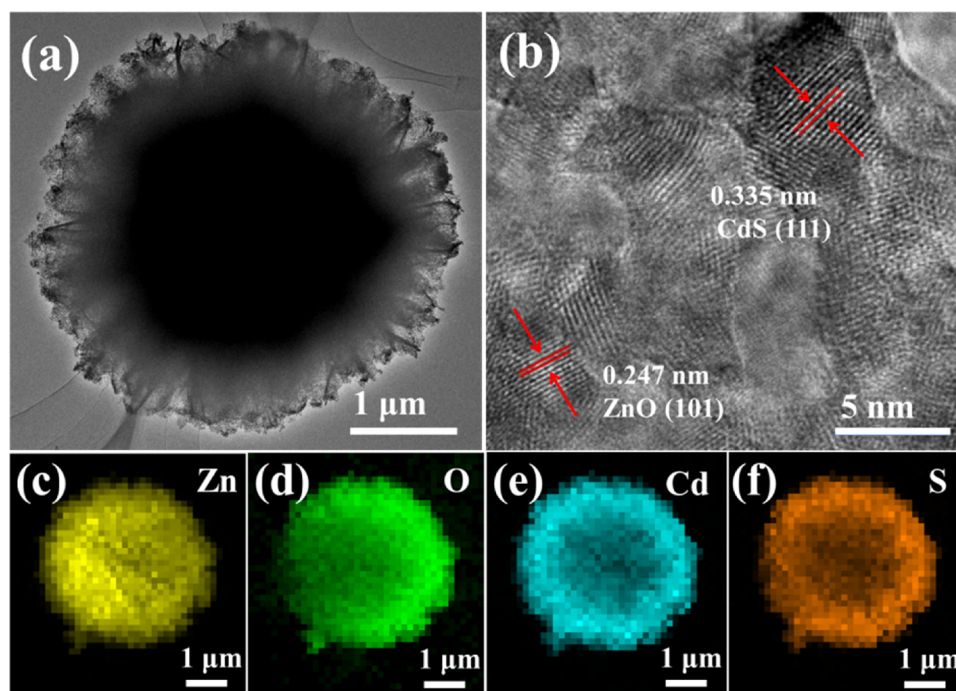


Fig. 4. (a) TEM, (b) HRTEM and (c–f) EDS mapping images of ZC-3.

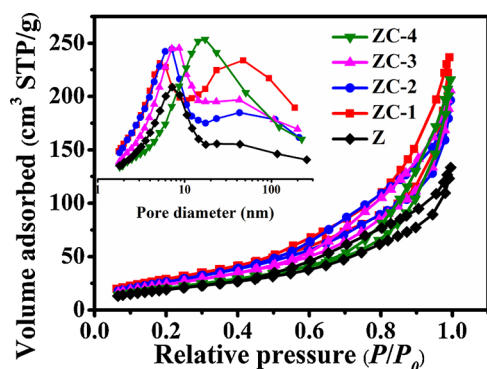
Fig. 5. N₂ adsorption-desorption isotherms and pore size distribution curves (inset) of different samples.

Table 2

Textural properties of different samples.

Samples	S_{BET} ($\text{m}^2 \text{g}^{-1}$)	V_p ($\text{cm}^3 \text{g}^{-1}$)	d_p (nm)
Z	73	0.2	11.2
ZC-1	80	0.33	16.7
ZC-2	94	0.32	13.6
ZC-3	103	0.31	11.7
ZC-4	112	0.37	13.0

Notes: SBET: BET specific surface area; V_p : pore volume; d_p : average pore size;

adsorption. The shortcoming of pristine ZnO, i.e. the poor adsorption in visible-light region is alleviated.

3.4. XPS analysis and DFT calculation

Fig. 7a and 7b show the high resolution XPS spectra of Zn and O elements in sample Z and ZC-3 with or without light irradiation. The detailed description can be found in the Experimental section. Without light irradiation, in comparison to the characteristic peaks of Zn ($2p_{3/2}$ and $2p_{1/2}$) and O (lattice oxygen and surface-adsorbed oxygen) of sample Z, both of those in ZC-3 shift negatively towards the lower

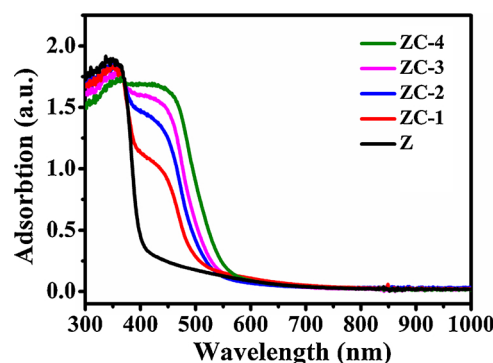


Fig. 6. Diffuse reflectance spectra of as-prepared samples.

energy direction [56,57]. By contrast, in comparison to the characteristic peaks of Cd ($3d_{5/2}$ and $3d_{3/2}$) and S, both of those in ZC-3 shift positively towards the higher energy direction (see Fig. 7c and 7d) [36]. Overall, the peak shifts of Zn 2p and O 1s are opposite to those of Cd 3d and S 2p. This indicates that the electrons migrate from the CdS to ZnO in sample ZC-3, which can be attributed to their different Fermi levels [58]. While the XPS analysis of different samples under light irradiation can be found in the following sections discussing the photocatalytic mechanism.

In order to further explore the charge migration between ZnO and CdS, the work functions of ZnO and CdS were calculated. In Fig. 8, the work functions of CdS (111) and ZnO (101) are 4.5 and 5.3 eV, respectively. These results reveal that ZnO (101) surface has lower Fermi level than CdS (111) surface. Consequently, as the CdS NPs come into contact with ZnO, the electrons will transfer from CdS to ZnO across their interface to find a balance of Fermi level between them, in accordance with the above XPS results. Then, the ZnO and CdS become negatively and positively charged, respectively. Thus, a built-in electric field was formed at the interface between ZnO and CdS.

3.5. Photoelectrochemical properties

In this section, to investigate the electron-hole separation efficiency,

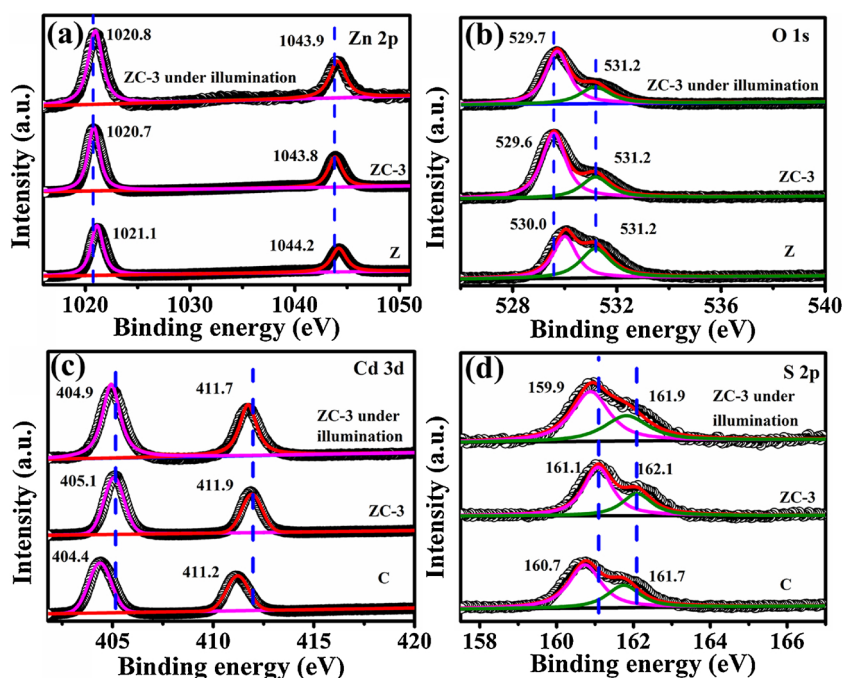


Fig. 7. XPS spectra of (a) Zn 2p; (b) O 1s; (c) Cd 3d and (d) S 2p.

we analyze the electrochemical impedance spectroscopy (EIS) and transient photocurrent response spectra of the samples. We performed several cycles tracking photocurrent of the sample under the intermittent illumination of UV-LED. As shown in Fig. 9a, when the light is switched on, the photocurrent rockets initially. This infers that the charge separation occurs between the sample and the electrolyte. Afterwards, the intensity of photocurrent dropped slightly due to the accumulation of holes. Generally speaking, instantaneous photocurrent response has a positive correlation with electron-hole separation efficiency of the sample, and the high separation efficiency contributes to better photocatalytic activity [59,60]. The photocurrent of composite samples is obviously higher than that of bare ZnO or CdS. This states the improved electron-hole separation efficiency of the composite samples. And Nyquist plots evaluating electrochemical impedance spectroscopy of these three samples are shown in Fig. 9b. The arc radius of the ZC-3 is smaller than that of ZnO or CdS sample, indicating that the charge transfer resistance of the composite sample is lower than that of the single component. In other words, the migration and separation of charges in the sample ZC-3 are more effective. All of these results point out the superiority of the composite over the single component in the electron-hole transportation and separation. The appropriate band positions of these two materials account for the enhanced charge separation, which allows the recombination of useless electrons and holes located in ZnO CB and CdS VB, respectively.

3.6. Photocatalytic performance

The photocatalytic activity of the sample was verified by decomposing water to produce hydrogen under light illumination. Prior to the experiments, hydrogen could not be detected in a series of blank control groups (without light or photocatalyst), indicating that light and photocatalyst are two indispensable prerequisites for hydrogen production. The H_2 -production performance of different samples can be clearly seen from Fig. 10a. Evidently, the pristine ZnO sample has barely any photocatalytic performance due to the rapid electron-hole recombination. Accompanied by the introduction of CdS, the hydrogen production rates of the samples soar sharply. This rate first boosts monotonically along with an increasing amount of CdS. And when the amount of CdS is about 30.9 wt%, the H_2 -production activity is the highest ($4134 \mu\text{mol g}^{-1} \text{h}^{-1}$). This increment is ascribed to the enhanced light adsorption and direct Z-scheme charge separation. It is worth noting that CdS loading has an optimal value. When the CdS loading exceeds a certain value, instead, the performance even degrades. Owing to the fact that ZnO is covered by CdS, the holes generated in ZnO need to pass through CdS to react with sacrificial agents. Namely, the direct contact between holes in ZnO and sacrificial agents is interrupted. Besides, when the holes thread in the CdS, they are prone to recombine with the electrons there. Hence, excessive CdS acts as an additional electron-hole recombination center, which in turn inhibits the photocatalytic activity

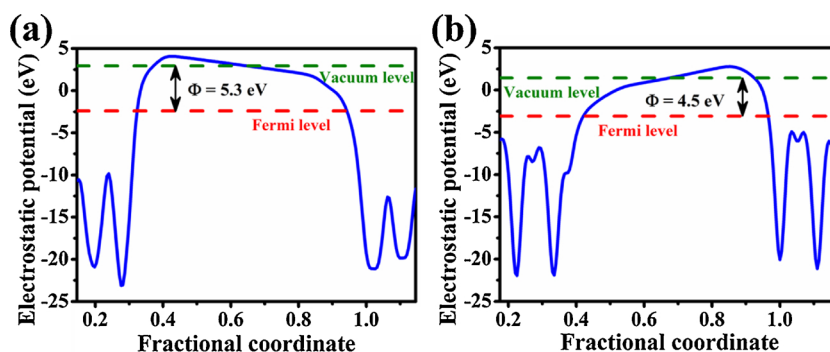


Fig. 8. Calculated Fermi levels and work functions of (a) ZnO (101) and (b) CdS (111) facets.

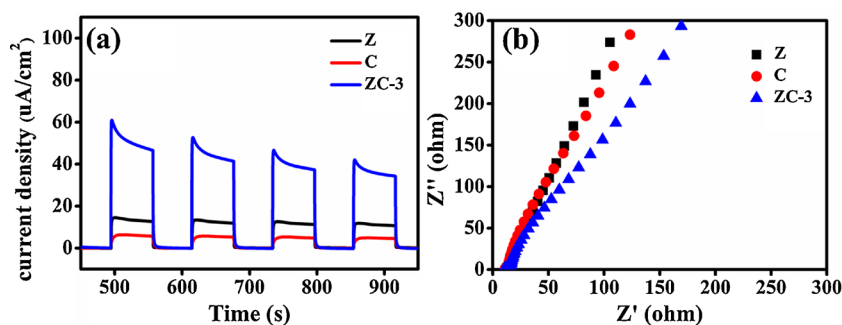


Fig. 9. (a) Transient photocurrent responses and (b) EIS Nyquist plots of sample Z, C and ZC-3 under light irradiation (365 nm).

of the sample. In addition, we conducted a cyclic H_2 -production experiment on the sample with the best performance (ZC-3). As shown in Fig. 10b, during the 18-hour cycling experiment, the photocatalyst can maintain high activity for 14 h. The deteriorated stability is due to the phase change after the cycling test, which was revealed by the XRD result (Fig. 11b). ZnS emerges after the cycling test, while the original ZnO disappeared. The above experimental results substantiate that the H_2 -production activity of ZnO can be greatly improved by loading CdS. And the ZnO/CdS composite is an effective photocatalytic H_2 -production material with reasonable stability.

3.7. Photocatalytic mechanism

Conventionally, two possible explanations for the electron-hole transport are widely accepted: (1) traditional Type-II and (2) direct Z-scheme heterojunction [61,62]. In the former, electrons move from a higher CB to a relatively lower CB; while holes move from a lower VB to a relatively higher VB. Thus, efficient separation of electrons and holes is achieved [63]. In contrast, with regard to the direct Z-scheme mechanism, electrons in the CB of one semiconductor and holes in the VB of another semiconductor with inferior redox powers recombine directly, and electrons and holes with better reduction and oxidation abilities are preserved [35,58]. According to previous analysis, the band edge positions of these two materials are shown in Fig. 11a. The VB potentials of ZnO and CdS are 3.0 and 1.88 V vs. NHE, respectively. Whereas the OH^-/OH position is about 2.8 V. It can be found that the VB position of CdS is higher than the OH^-/OH position, unable to produce $\cdot\text{OH}$. The CB positions of ZnO and CdS are at -0.2 and -0.42 V, respectively, and both of them are higher than the H^+/H_2 position. It is therefore difficult to ascertain the exact mechanism by simply judging from the hydrogen production since hydrogen can be produced by either mechanism. We used the generation of $\cdot\text{OH}$ to identify which mechanism applies for our hybrid. Terephthalic acid was selected as the trapping agent for the $\cdot\text{OH}$. The feasibility of this approach is

elaborated in Fig. 11a, where the band edge positions of each component, hydrogen production potential and the OH^-/OH potential are displayed. The VB potential of CdS (1.88 V) is more negative than the OH^-/OH potential (2.8 V), if Type-II heterojunction is correct, the composite sample ZC-3 cannot produce $\cdot\text{OH}$. Otherwise, if direct Z-scheme is valid, $\cdot\text{OH}$ can be detected.

In Fig. 12b, PL signals of pure ZnO and ZC-3 samples are obvious under the light illumination, and that of the pristine CdS sample is very weak. The reason why a faint PL signal can be detected in CdS sample may be that the $\cdot\text{OH}$ is not generated directly, but rather it is derived from the indirect conversion of $\cdot\text{O}_2^-$ generated on the CdS conduction band [9,58]. Therefore, direct Z-scheme mechanism is indirectly supported by the $\cdot\text{OH}$ probe. Namely, under light illumination, electrons in the VB of ZnO and CdS are excited to their respective CB, leaving holes in the VB. Subsequently, subjected to the built-in electric field, electrons in the ZnO CB recombine with the holes in CdS VB, leaving electrons in the CdS CB and holes in the ZnO VB. The potential of the ZnO VB is more positive than the OH^-/OH potential, and thus it can produce $\cdot\text{OH}$, which is in agreement with the above experimental results. In hydrogen production experiments, holes in the ZnO VB are consumed by sacrificial agents, holes react with S^{2-} , SO_3^{3-} generate SO_4^{2-} and $\text{S}_2\text{O}_3^{3-}$, electrons in the CdS CB react with H^+ to form H_2 .

The direct Z-scheme charge transfer was further corroborated by *in-situ* XPS measurement under light illumination. As shown in Fig. 7a and b, on one hand, under light illumination, the binding energies of Zn 2p and O 1s (lattice oxygen) in ZC-3 increase about 0.1 eV in comparison with the values measured in dark. On the other hand, under light illumination, the binding energies of Cd 3d and S 2p (Fig. 7c and d) in ZC-3 decrease about 0.2 eV, compared with the values tested in dark. The above *in-situ* XPS results indicate that the electrons transfer from ZnO to CdS under light illumination, which is in accordance with the direct Z-scheme mechanism.

Above all, we proposed and validated the direct Z-scheme pathway to clarify the improved photocatalytic H_2 -production activity of the hybrid material ZnO/CdS.

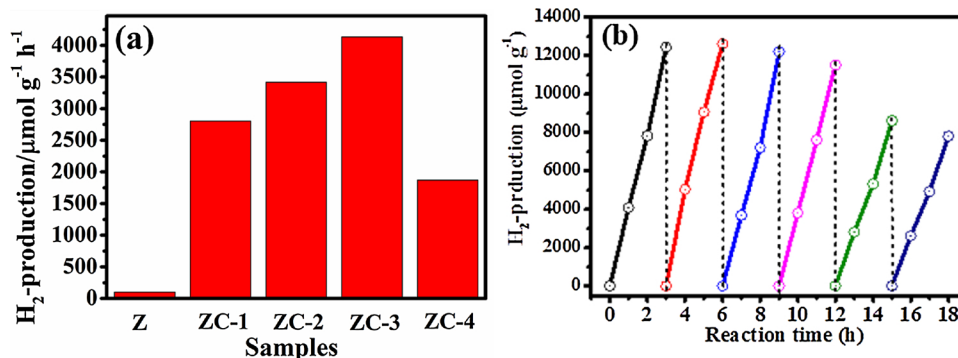


Fig. 10. (a) Photocatalytic activities for various samples and (b) cycling stability for sample ZC-3.

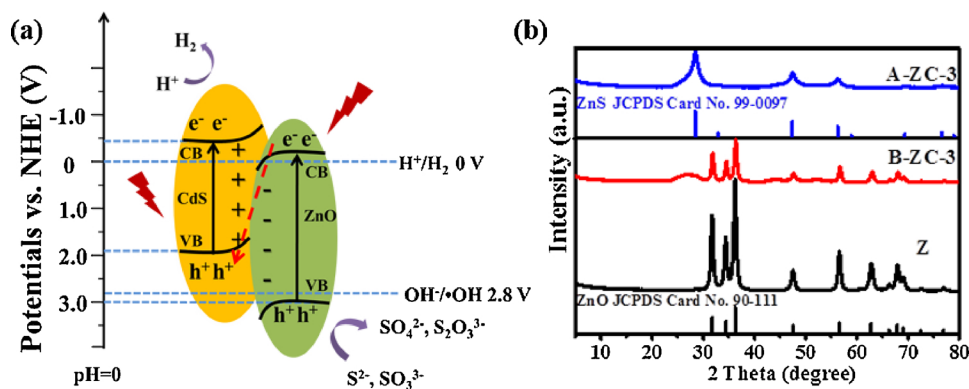


Fig. 11. (a) Schematic diagram of direct Z-scheme pathway for charge carrier separation, (b) XRD results before (B-ZC-3) and after (A-ZC-3) cycling tests of ZC-3 in comparison to the XRD spectrum of Z (ZnO).

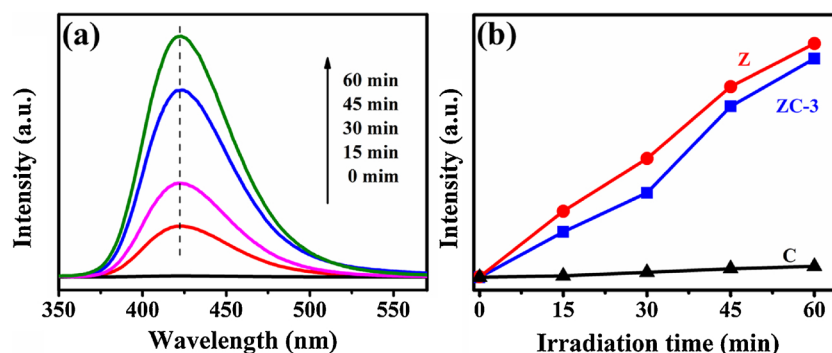


Fig. 12. (a) PL spectral changes at different time for the ZC-3 sample under illumination in a mixed solution with TA (0.5 mM) and NaOH (2 mM); (b) PL peak intensity (423 nm) for different samples against irradiation time.

4. Conclusions

Herein, ZnO microspheres were fabricated by a hydrothermal process; and afterwards, CdS NPs were deposited on their surface through a chemical bath deposition method, obtaining ZnO/CdS hybrid. The experimental results show that the CdS loading has an optimal value because excessive CdS will act as an electron-hole recombination center. When the mass ratio of CdS is 30.9%, the composite has the best photocatalytic hydrogen-generation performance ($4134 \mu\text{mol g}^{-1} \text{h}^{-1}$). The introduction of CdS greatly improves the absorption of ZnO in the visible region and the photoelectron-hole separation efficiency. The *in-situ* XPS measurement, hydroxyl radical detection experiment and the work function calculation have certified the direct Z-scheme charge-transfer mechanism between ZnO and CdS under light illumination. And this direct Z-scheme mechanism greatly improved the photocatalytic performance.

Acknowledgements

This work was supported by NSFC (51320105001, U1705251, 21433007 and 21573170), Natural Science Foundation of Hubei Province (2015CFA001) and Innovative Research Funds of SKLWUT (2017-ZD-4).

References

- [1] E. Aslan, O. Birinci, A. Aljabour, F. Ozel, I. Akin, I.H. Patir, M. Kus, M. Ersoz, Photocatalytic hydrogen evolution by oleic acid-capped CdS, CdSe, and $\text{CdS}_{0.75}\text{Se}_{0.25}$ alloy nanocrystals, *ChemPhysChem* 15 (2014) 2668–2671.
- [2] H. Zhao, X. Ding, B. Zhang, Y. Li, C. Wang, Enhanced photocatalytic hydrogen evolution along with byproducts suppressing over Z-scheme $\text{Cd}_x\text{Zn}_{1-x}\text{S}/\text{Au}/\text{g-C}_3\text{N}_4$ photocatalysts under visible light, *Sci. Bull.* 62 (2017) 602–609.
- [3] D. Wu, F. Wang, Y. Tan, C. Li, Facile synthesis of NiS/CdS nanocomposites for photocatalytic degradation of quinoline under visible-light irradiation, *RSC Adv.* 6 (2016) 73522–73526.
- [4] L. Cui, X. Ding, Y. Wang, H. Shi, L. Huang, Y. Zuo, S. Kang, Facile preparation of Z-scheme $\text{WO}_3/\text{g-C}_3\text{N}_4$ composite photocatalyst with enhanced photocatalytic performance under visible light, *Appl. Surf. Sci.* 391 (2017) 202–210.
- [5] J. Li, M. Zhang, Q. Li, J. Yang, Enhanced visible light activity on direct contact Z-scheme $\text{g-C}_3\text{N}_4\text{-TiO}_2$ photocatalyst, *Appl. Surf. Sci.* 391 (2017) 184–193.
- [6] A. Fujishima, K. Honda, Electrochemical photolysis of water at a semiconductor electrode, *Nature* 238 (1972) 37–38.
- [7] P. Wang, Q. Zhou, Y. Xia, S. Zhan, Y. Li, Understanding the charge separation and transfer in mesoporous carbonate doped phase-junction TiO_2 nanotubes for photocatalytic hydrogen production, *Appl. Catal. B* 225 (2018) 433–444.
- [8] H. Wang, W. Zheng, W. Li, F. Tian, S. Kuang, Y. Bu, J.-P. Ao, Control the energy band potential of ZnMgO solid solution with enhanced photocatalytic hydrogen evolution capacity, *Appl. Catal. B* 217 (2017) 523–529.
- [9] A. Meng, J. Zhang, D. Xu, B. Cheng, J. Yu, Enhanced photocatalytic H_2 -production activity of anatase TiO_2 nanosheet by selectively depositing dual-cocatalysts on {101} and {001} facets, *Appl. Catal. B* 198 (2016) 286–294.
- [10] A.L. Luna, E. Novoseltceva, E. Louarn, P. Beaudier, E. Kowalska, B. Ohtani, M.A. Valenzuela, H. Remita, C. Colbeau-Justin, Synergetic effect of Ni and Au nanoparticles synthesized on titania particles for efficient photocatalytic hydrogen production, *Appl. Catal. B* 191 (2016) 18–28.
- [11] T. Wang, W. Li, D. Xu, X. Wu, L. Cao, J. Meng, A novel and facile synthesis of black TiO_2 with improved visible-light photocatalytic H_2 generation: impact of surface modification with CTAB on morphology, structure and property, *Appl. Surf. Sci.* 426 (2017) 325–332.
- [12] J. Fu, J. Yu, C. Jiang, B. Cheng, Gg- C_3N_4 -based heterostructured photocatalysts, *Adv. Eng. Mater.* 8 (2018) 1701503.
- [13] S.O. Oseni, K. Kaviyarasu, M. Maaza, G. Sharma, G. Pellicane, G.T. Mola, ZnO:CNT assisted charge transport in PTB7:PCBM blend organic solar cell, *J. Alloys Compd.* 748 (2018) 216–222.
- [14] C. Lei, M. Pi, C. Jiang, B. Cheng, J. Yu, Synthesis of hierarchical porous zinc oxide (ZnO) microspheres with highly efficient adsorption of Congo red, *J. Colloid Interface Sci.* 490 (2017) 242–251.
- [15] N. Nie, L. Zhang, J. Fu, B. Cheng, J. Yu, Self-assembled hierarchical direct Z-scheme $\text{g-C}_3\text{N}_4/\text{ZnO}$ microspheres with enhanced photocatalytic CO_2 reduction performance, *Appl. Surf. Sci.* 441 (2018) 12–22.
- [16] K. Qi, B. Cheng, J. Yu, W. Ho, Review on the improvement of the photocatalytic and antibacterial activities of ZnO, *J. Alloys Compd.* 727 (2017) 792–820.
- [17] W. Yu, J. Zhang, T. Peng, New insight into the enhanced photocatalytic activity of N-, C- and S-doped ZnO photocatalysts, *Appl. Catal. B* 181 (2016) 220–227.
- [18] T. Di, B. Zhu, J. Zhang, B. Cheng, J. Yu, Enhanced photocatalytic H_2 production on CdS nanorod using cobalt-phosphate as oxidation cocatalyst, *Appl. Surf. Sci.* 389 (2016) 73522–73526.

- (2016) 775–782.
- [19] Z. Jiang, J. Liu, M. Gao, X. Fan, L. Zhang, J. Zhang, Assembling polyoxo-titanium clusters and CdS nanoparticles to a porous matrix for efficient and tunable H₂-evolution activities with visible light, *Adv. Mater.* 29 (2017) 1603369.
 - [20] Q. Li, X. Li, S. Wageh, A.A. Al-Ghamdi, J. Yu, CdS/graphene nanocomposite photocatalysts, *Adv. Eng. Mater.* 5 (2015) 1500010.
 - [21] A. Vazquez, D.B. Hernandez-Uresti, S. Obregon, Electrophoretic deposition of CdS nanoparticles and their photocatalytic activities in the degradation of tetracycline antibiotic, *Appl. Surf. Sci.* 386 (2016) 412–417.
 - [22] D. You, B. Pan, F. Jiang, Y. Zhou, W. Su, CdS nanoparticles/CeO₂ nanorods composite with high-efficiency visible-light-driven photocatalytic activity, *Appl. Surf. Sci.* 363 (2016) 154–160.
 - [23] X. Yin, G. He, B. Sun, W. Jiang, D. Xue, A. Xia, L. Wan, J. Hu, Rational design and electron transfer kinetics of MoS₂/CdS nanodots-on-nanorods for efficient visible-light-driven hydrogen generation, *Nano Energy* 28 (2016) 319–329.
 - [24] R.M. Irfan, D. Jiang, Z. Sun, D. Lu, P. Du, Enhanced photocatalytic H₂ production on CdS nanorods with simple molecular bidentate cobalt complexes as cocatalysts under visible light, *Dalton Trans.* 45 (2016) 12897–12905.
 - [25] S. Ijaz, M.F. Ehsan, M.N. Ashiq, N. Karamat, T. He, Preparation of CdS@CeO₂ core/shell composite for photocatalytic reduction of CO₂ under visible-light irradiation, *Appl. Surf. Sci.* 390 (2016) 550–559.
 - [26] J. Yu, S. Wang, J. Low, W. Xiao, Enhanced photocatalytic performance of direct Z-scheme g-C₃N₄-TiO₂ photocatalysts for the decomposition of formaldehyde in air, *Phys. Chem. Chem. Phys.* 15 (2013) 16883–16890.
 - [27] Z. Wang, T. Hu, K. Dai, J. Zhang, C. Liang, Construction of Z-scheme Ag₃PO₄/Bi₂WO₆ composite with excellent visible-light photodegradation activity for removal of organic contaminants, *Chin. J. Catal.* 38 (2017) 2021–2029.
 - [28] Y. Fu, Z. Li, Q. Liu, X. Yang, H. Tang, Construction of carbon nitride and MoS₂ quantum dot 2D/0D hybrid photocatalyst: direct Z-scheme mechanism for improved photocatalytic activity, *Chin. J. Catal.* 38 (2017) 2160–2170.
 - [29] C. Song, X. Wang, J. Zhang, X. Chen, C. Li, Enhanced performance of direct Z-scheme CuS-WO₃ system towards photocatalytic decomposition of organic pollutants under visible light, *Appl. Surf. Sci.* 425 (2017) 788–795.
 - [30] W. Liu, L. Qiao, A. Zhu, Y. Liu, J. Pan, Constructing 2D BiOCl/C₃N₄ layered composite with large contact surface for visible-light-driven photocatalytic degradation, *Appl. Surf. Sci.* 426 (2017) 897–905.
 - [31] D. Chen, J. Fang, S. Lu, G. Zhou, W. Feng, F. Yang, Y. Chen, Z. Fang, Fabrication of Bi modified Bi₂S₃ pillared g-C₃N₄ photocatalyst and its efficient photocatalytic reduction and oxidation performances, *Appl. Surf. Sci.* 426 (2017) 427–436.
 - [32] H.H. El-Maghrabi, A. Barhoum, A.A. Nada, Y.M. Moustafa, S.M. Seliman, A.M. Youssef, M. Bechelany, Synthesis of mesoporous core-shell CdS@TiO₂ (0D and 1D) photocatalysts for solar-driven hydrogen fuel production, *J. Photochem. Photobiol. A Chem.* 351 (2018) 261–270.
 - [33] R. Shi, P. Yang, X. Song, J. Wang, Q. Che, A. Zhang, ZnO flower: self-assembly growth from nanosheets with exposed {1 1 $\bar{0}$ 0} facet, white emission, and enhanced photocatalysis, *Appl. Surf. Sci.* 366 (2016) 506–513.
 - [34] J. Qin, X. Zhang, C. Yang, M. Cao, M. Ma, R. Liu, ZnO microspheres-reduced graphene oxide nanocomposite for photocatalytic degradation of methylene blue dye, *Appl. Surf. Sci.* 392 (2017) 196–203.
 - [35] J. Jin, J. Yu, D. Guo, C. Cui, W. Ho, A hierarchical Z-scheme CdS-WO₃ photocatalyst with enhanced CO₂ reduction activity, *Small* 11 (2015) 5262–5271.
 - [36] A. Meng, B. Zhu, B. Zhong, L. Zhang, B. Cheng, Direct Z-scheme TiO₂/CdS hierarchical photocatalyst for enhanced photocatalytic H₂-production activity, *Appl. Surf. Sci.* 422 (2017) 518–527.
 - [37] Q. Xu, B. Zhu, C. Jiang, B. Cheng, J. Yu, Constructing 2D/2D Fe₂O₃/g-C₃N₄ direct Z-scheme photocatalysts with enhanced H₂ generation performance, *Sol. RRL* 2 (2018) 1800006.
 - [38] J. Low, C. Jiang, B. Cheng, S. Wageh, A.A. Al-Ghamdi, J. Yu, A review of direct Z-scheme photocatalysts, *Small Methods* 1 (2017) 1700080.
 - [39] K. Qi, B. Cheng, J. Yu, W. Ho, A review on TiO₂-based Z-scheme photocatalysts, *Chin. J. Catal.* 38 (2017) 1936–1955.
 - [40] J. Liu, B. Cheng, J. Yu, A new understanding of the photocatalytic mechanism of the direct Z-scheme g-C₃N₄/TiO₂ heterostructure, *Phys. Chem. Chem. Phys.* 18 (2016) 31175–31183.
 - [41] Q. Xu, L. Zhang, J. Yu, S. Wageh, A.A. Al-Ghamdi, M. Jaroniec, Direct Z-scheme photocatalysts: principles, synthesis, and applications, *Mater. Today* (2018), <https://doi.org/10.1016/j.mattod.2018.04.008>.
 - [42] W. Yu, J. Chen, T. Shang, L. Chen, L. Gu, T. Peng, Direct Z-scheme g-C₃N₄/WO₃ photocatalyst with atomically defined junction for H₂ production, *Appl. Catal. B* 219 (2017) 693–704.
 - [43] M.E. Aguirre, R. Zhou, A.J. Eugene, M.I. Guzman, M.A. Grela, Cu₂O/TiO₂ heterostructures for CO₂ reduction through a direct Z-scheme: protecting Cu₂O from photocorrosion, *Appl. Catal. B* 217 (2017) 485–493.
 - [44] M. Akbari, S. Sharifnia, Synthesis of ZnS/ZnO nanocomposite through solution combustion method for high rate photocatalytic conversion of CO₂ and CH₄, *Mater. Lett.* 194 (2017) 110–113.
 - [45] Y. Al-Hadeethi, A. Umar, S.H. Al-Heniti, R. Kumar, S.H. Kim, X. Zhang, B.M. Raffah, 2D Sn-doped ZnO ultrathin nanosheet networks for enhanced acetone gas sensing application, *Ceram. Int.* 43 (2017) 2418–2423.
 - [46] S. Cao, X. Yan, Z. Kang, Q. Liang, X. Liao, Y. Zhang, Band alignment engineering for improved performance and stability of ZnFe₂O₄ modified CdS/ZnO nanostructured photoanode for PEC water splitting, *Nano Energy* 24 (2016) 25–31.
 - [47] H. Shima, M.M. Hossain, I. Lee, S. Son, J.R. Hahn, Carbon-ZnO core-shell nanoparticles: facile fabrication and application in the visible-light photocatalytic decomposition of organic pollutant dyes, *Mater. Chem. Phys.* 185 (2017) 73–82.
 - [48] S. Bai, J. Guo, X. Shu, X. Xiang, R. Luo, D. Li, A. Chen, C. Liu, Surface functionalization of Co₃O₄ hollow spheres with ZnO nanoparticles for modulating sensing properties of formaldehyde, *Sens. Actuators B: Chem.* 245 (2017) 359–368.
 - [49] M. Thommes, K. Kaneko, A.V. Neimark, J.P. Olivier, F. Rodriguez-Reinoso, J. Rouquerol, K.S.W. Sing, Physisorption of gases, with special reference to the evaluation of surface area and pore size distribution (IUPAC technical report), *Pure Appl. Chem.* 87 (2015) 1051–1069.
 - [50] K.N. Abbas, N. Bidin, Morphological driven photocatalytic activity of ZnO nanostructures, *Appl. Surf. Sci.* 394 (2017) 498–508.
 - [51] D. Xu, B. Cheng, S. Cao, J. Yu, Enhanced photocatalytic activity and stability of Z-scheme Ag₂CrO₄-GO composite photocatalysts for organic pollutant degradation, *Appl. Catal. B* 164 (2015) 380–388.
 - [52] H. Zhang, G. Du, W. Lu, L. Cheng, X. Zhu, Z. Jiao, Porous TiO₂ hollow nanospheres: synthesis, characterization and enhanced photocatalytic properties, *CrystEngComm* 14 (2012) 3793–3801.
 - [53] S. Akir, A. Barras, Y. Coffinier, M. Bououdina, R. Boukherroub, A.D. Omrani, Eco-friendly synthesis of ZnO nanoparticles with different morphologies and their visible light photocatalytic performance for the degradation of rhodamine B, *Ceram. Int.* 42 (2016) 10259–10265.
 - [54] R. Lei, H. Ni, R. Chen, H. Gu, B. Zhang, W. Zhan, Hydrothermal synthesis of CdS nanorods anchored on alpha-Fe₂O₃ nanotube arrays with enhanced visible-light-driven photocatalytic properties, *J. Colloid Interface Sci.* 514 (2018) 496–506.
 - [55] Z. Bai, X. Yan, Y. Li, Z. Kang, S. Cao, Y. Zhang, 3D-branched ZnO/CdS nanowire arrays for solar water splitting and the service safety research, *Adv. Eng. Mater.* 6 (2016) 1501459.
 - [56] S. Wang, P. Kuang, B. Cheng, J. Yu, C. Jiang, ZnO hierarchical microsphere for enhanced photocatalytic activity, *J. Alloys Compd.* 741 (2018) 622–632.
 - [57] T. Chen, S. Yu, X. Fang, H. Huang, L. Li, X. Wang, H. Wang, Enhanced photocatalytic activity of C@ZnO core-shell nanostructures and its photoluminescence property, *Appl. Surf. Sci.* 389 (2016) 303–310.
 - [58] W. Yu, D. Xu, T. Peng, Enhanced photocatalytic activity of g-C₃N₄ for selective CO₂ reduction to CH₃OH via facile coupling of ZnO: a direct Z-scheme mechanism, *J. Mater. Chem. A* 3 (2015) 19936–19947.
 - [59] S. Le, T. Jiang, Y. Li, Q. Zhao, Y. Li, W. Fang, M. Gong, Highly efficient visible-light-driven mesoporous graphitic carbon nitride/ZnO nanocomposite photocatalysts, *Appl. Catal. B* 200 (2017) 601–610.
 - [60] L. Zhang, L. Li, X. Sun, P. Liu, D. Yang, X. Zhao, ZnO-layered double hydroxide/graphitic carbon nitride composite for consecutive adsorption and photodegradation of dyes under UV and visible lights, *Materials* 9 (2016) 927.
 - [61] J.-C. Wang, H.-C. Yao, Z.-Y. Fan, L. Zhang, J.-S. Wang, S.-Q. Zang, Z.-J. Li, Indirect Z-Scheme BiOI/g-C₃N₄ photocatalysts with enhanced photoreduction CO₂ activity under visible light irradiation, *ACS Appl. Mater. Interfaces* 8 (2016) 3765–3775.
 - [62] J.-C. Wang, L. Zhang, W.-X. Fang, J. Ren, Y.-Y. Li, H.-C. Yao, J.-S. Wang, Z.-J. Li, Enhanced photoreduction CO₂ activity over direct Z-Scheme α -Fe₂O₃/Cu₂O heterostructures under visible light irradiation, *ACS Appl. Mater. Interfaces* 7 (2015) 8631–8639.
 - [63] L. Wang, C. Ma, Z. Guo, Y. Lv, W. Chen, Z. Chang, Q. Yuan, H. Ming, J. Wang, In-situ growth of g-C₃N₄ layer on ZnO nanoparticles with enhanced photocatalytic performances under visible light irradiation, *Mater. Lett.* 188 (2017) 347–350.